Journal of
Synchrotron
Radiation

ISSN 0909-0495

Received 22 July 2011
Accepted 23 September 2011

A furnace and environmental cell for the *in situ* investigation of molten salt electrolysis using high-energy X-ray diffraction

Mark J. Styles,[a]* Matthew R. Rowles,[a,b] Ian C. Madsen,[b] Katherine McGregor,[b] Andrew J. Urban,[b] Graeme A. Snook,[b] Nicola V. Y. Scarlett[b] and Daniel P. Riley[a,c]

[a]Department of Mechanical Engineering, The University of Melbourne, Parkville, Victoria 3010, Australia, [b]CSIRO Process Science and Engineering, Box 312, Clayton South, Victoria 3168, Australia, and [c]ANSTO Institute of Materials Engineering, Locked Bag 2001, Kirrawee DC, NSW 2232, Australia. E-mail: mark.styles@csiro.au

This paper describes the design, construction and implementation of a relatively large controlled-atmosphere cell and furnace arrangement. The purpose of this equipment is to facilitate the *in situ* characterization of materials used in molten salt electrowinning cells, using high-energy X-ray scattering techniques such as synchrotron-based energy-dispersive X-ray diffraction. The applicability of this equipment is demonstrated by quantitative measurements of the phase composition of a model inert anode material, which were taken during an *in situ* study of an operational Fray–Farthing–Chen Cambridge electrowinning cell, featuring molten $CaCl_2$ as the electrolyte. The feasibility of adapting the cell design to investigate materials in other high-temperature environments is also discussed.

© 2012 International Union of Crystallography
Printed in Singapore – all rights reserved

Keywords: X-ray diffraction; energy dispersive; *in situ*; molten salt; electrolysis.

1. Introduction

Since its introduction in the late 19th century, molten salt electrolysis has become a key technology in the field of extractive metallurgy. It is currently used extensively in the production of light metals such as aluminium, lithium and magnesium (Habashi, 1997), and there are on-going efforts to replace the Kroll process for titanium production (Kroll, 1940) with a more cost-effective electrolytic route (Ginatta, 2000; Kraft, 2004; Fray, 2008). Despite the maturity and widespread use of molten salt electrolysis, substantial differences still remain between the theoretical efficiencies of individual processes and those that can be achieved in practice (Fray, 2001; Evans, 2007). In many cases this disparity can be attributed to design and operational limitations that are imposed by the almost ubiquitous use of graphitic carbon electrodes and cell linings (Zhang *et al.*, 1994; Galasiu *et al.*, 2007; Dow Chemical Company, 1997; Jiao & Fray, 2010), which often react undesirably with process materials such as the electrolyte and electrode products, and require frequent replacement. However, even after decades of research, no economically viable alternatives to these carbon-based materials have been identified (Pawlek, 2008, 2010). In order to develop new cell materials, a more detailed understanding of the structural and chemical changes that lead to the failure of potential carbon alternatives is needed.

To date, the development of new cell materials has relied on the characterization of samples which have been removed from their operational environment at various pre-defined points of interest (McGregor *et al.*, 2006). This *ex situ* approach can be problematic as conventional analysis techniques typically require some form of sample preparation, which can range from simply allowing the sample to cool, to more invasive procedures such as cutting and polishing. While any material studied outside of its operational environment will be altered to some extent, such treatment is particularly damaging to friable surface layers, layers that have been found to be crucial to the performance and longevity of components used within the highly corrosive environment of a molten salt cell (McGregor *et al.*, 2006). Obtaining clear information about how these surface layers evolve during cell operation, without disrupting their fragile structure, requires the use of an *in situ* characterization method.

Modern synchrotron and neutron powder diffraction techniques are well suited to *in situ* studies of solid-state reactions, owing to their ability to provide quantitative phase information with the time resolution needed to investigate kinetics and other rate-limiting phenomena (Cheetham & Mellot, 1997; Norby *et al.*, 2000; Walton & O'Hare, 2000; Riley *et al.*, 2002; Scarlett *et al.*, 2008). However, the complexity of the environmental equipment required to accurately and safely imitate an operational molten salt cell is challenging for many

diffraction techniques. First, a very penetrating radiation must be used in order to pass through the walls of the containment vessel as well as several centimetres of absorbing electrolyte. Second, high spatial resolution is required to selectively study the component of interest, such as the anode, in a multi-component system. Considering these requirements, it would be very difficult to apply *in situ* neutron diffraction techniques to the study of operational molten salt electrowinning cells, even using sample environment equipment that has been customized to suit neutron scattering experiments (Styles & Riley, 2010; Styles *et al.*, 2009). This is due to the necessity to compromise between the temporal and spatial resolution of measurements made with neutrons and the substantial limitations that are imposed, by monochromatic diffraction techniques in particular, on the design of reaction vessels. Synchrotron-based energy-dispersive X-ray diffraction (EDXRD), however, is uniquely capable as its characteristics include (i) penetrating high-energy X-rays (>40 keV), (ii) a fixed detector position, allowing tight collimation of the diffracted beam, thus providing good spatial resolution, and (iii) a very high intensity beam which allows for short data acquisition times (Buras *et al.*, 1976; Häusermann & Barnes, 1992; Clark, 2002). This technique, shown schematically in Fig. 1, has been successfully employed in a number of studies of reacting systems that have required substantial sample environment equipment (Barnes *et al.*, 1992; Clark *et al.*, 1995; Francis & O'Hare, 1998). Importantly, analysis techniques to extract accurate quantitative phase information from EDXRD data, using a whole-pattern Rietveld-based approach, have recently been developed (Scarlett *et al.*, 2009; Rowles *et al.*, 2011*a*).

The design of a novel molten salt electrowinning cell and a customized tube furnace, capable of simulating a variety of different molten salt processes in a manner that is compatible with synchrotron-based EDXRD, is reported here. The performance of this new equipment is demonstrated by an *in situ* EDXRD study (Rowles *et al.*, 2011*b*) of the growth of electrically insulating layers on the surface of a model inert anode material within an operational Fray–Farthing–Chen Cambridge (FFC) (Chen *et al.*, 2000) style titanium electro-

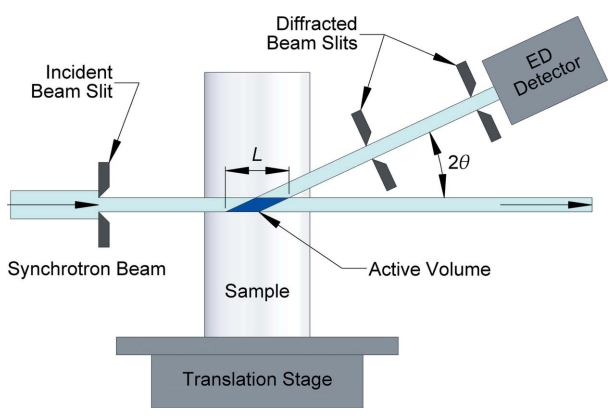

Figure 1
Schematic representation of the energy-dispersive X-ray diffraction technique, showing the arrangement of incident and diffracted beam slits used to define an active volume of length *L*.

winning cell. The implications of this research are important, as the lack of a suitably inert alternative to carbon anodes is a significant factor preventing the FFC process from competing with the existing Kroll process (Jiao & Fray, 2010). The feasibility of adapting this cell design to study other molten salt processes is also discussed.

2. Electrowinning cell and furnace design

The FFC process is a form of molten salt electrolysis which aims to produce titanium and titanium-based alloys directly from oxide precursors (Chen *et al.*, 2000; Bertolini *et al.*, 2010). The process essentially operates by suspending solid pellets of TiO_2 in a bath of molten $CaCl_2$, using a suitably inert wire that acts as the cathodic current collector. In the present study the conventional graphite anode is replaced with an electrically conductive ceramic situated near the surface of the electrolyte. When a voltage is applied across the electrodes, O^{2-} ions are stripped from the pellets and transported through the $CaCl_2$ to the anode, where they react to form a gaseous product (O_2, or CO_2 if graphite is used as the anode material) that leaves the cell in a flowing stream of argon. As the process operates at about 1223 K, the electrowon titanium remains solid and can easily be removed from the cell under an inert argon atmosphere.

The essential components required to construct an FFC cell, and indeed most other molten salt electrowinning cells, include: (i) an anode; (ii) a cathode; (iii) a volume of molten electrolyte in contact with both the anode and the cathode; (iv) a containment vessel/crucible; (v) an inert cover gas; (vi) a controlled source of DC electrical current; (vii) a controlled heat source.

The cell design described in §2.1 implements components (i) to (v), in a manner suited to studying the FFC process. The source of electrical current for this equipment is a standard electrochemical potentiostat, such as the PAR 362 used in the experiment described in §3, which only requires that the cell feature standard electrode terminals such as 4 mm banana plugs. The heat source for this cell is the vertical tube furnace described in §2.2.

2.1. Electrowinning cell

The guiding principle behind the design of the cell presented here was to enable *in situ* characterization of cell components using EDXRD, without compromising the electrochemical reactions at either the anode or cathode. In general, laboratory equipment such as that described by McGregor *et al.* (2006) can easily be used to achieve an accurate electrode environment. However, the bulky nature of this equipment is rarely compatible with synchrotron techniques. In contrast, cells such as those described by Evans *et al.* (1995) and Geselbracht *et al.* (2000) have been designed specifically for EDXRD experiments but cannot accommodate sample environments of the size and complexity needed to accurately simulate industrial electrochemical processes. Jackson *et al.* (2010) have also studied the FFC

process using *in situ* EDXRD. However, their cell had been optimized specifically for investigating cathode reaction mechanisms. A major goal in the design of the cell presented here was to incorporate features that allow for the straightforward investigation of *both* the anode and the cathode. To facilitate this, the cell has been separated into three distinct assemblies: an electrode stalk, a cell body and a cell head.

2.1.1. Electrode stalk. To ensure that the environments surrounding the electrodes are as representative of the FFC process as possible, a sample-outward approach was taken during the design of the cell. In this regard the anode holder (Fig. 2) is the most critical component in the electrowinning cell, as it influences the positioning of every other component and therefore controls the overall diameter of the cell. It is constructed from a 10 mm-diameter stainless steel rod, with a slot 3.4 mm wide wire-cut in one end to form the tines used to grip the ceramic anode. A thinner (∼1 mm) slot cut further up the rod allows a countersunk screw to clamp the two tines closed on the anode. The other end of the anode holder features a threaded hole with milled flats to allow the use of a spanner during assembly of the electrode stalk. In order to connect the anode holder to the leads of the power supply, a 6 mm-diameter by 490 mm-long stainless steel rod is used. This has an M6 thread tapped on one end and an M4 hole bored in the other to allow connection to the banana plugs from the power supply. These steel components are sheathed in alumina to protect them from the oxidizing environment and to prevent them from contacting other conductive materials. The sheath over the 6 mm rod has a 1/4-inch internal diameter to allow for thermal expansion and is bonded to the rod over the upper 200 mm using Ceramabond 671 (Aremco Products).

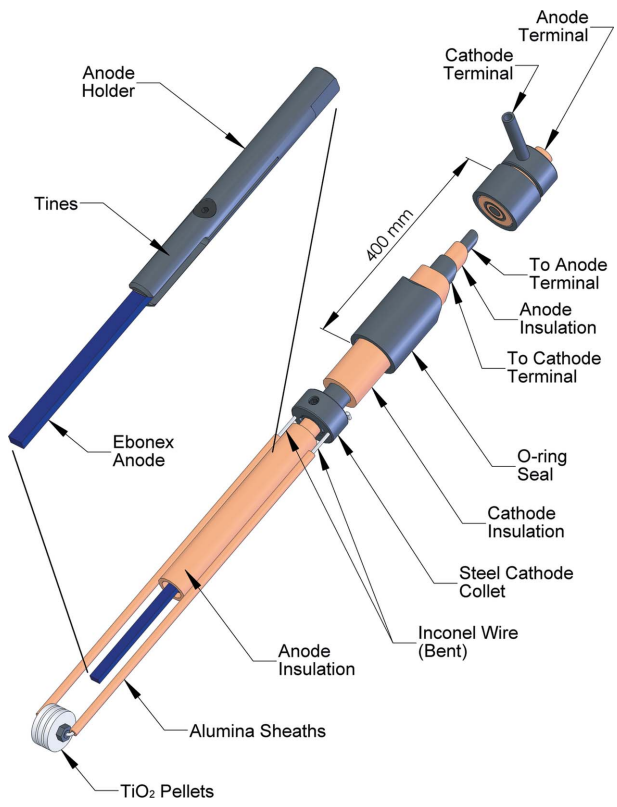

Figure 2
Overview of the electrode stalk described in the text, highlighting the location of key features. All metal components are electrically insulated from one another using alumina sheaths. The anode holder is shown enlarged in the upper portion of the diagram.

Sintered TiO_2 pellets that can be inserted and removed with each anode sample are used as the cathode material in this cell. Three 1 g pellets, ∼15 mm in diameter by 2 mm thick, are supported on a short-length stainless steel rod machined with an M4 thread on the outside and bored through with a 1.8 mm hole. These pellets are separated with stainless steel washers and gently clamped in place with M4 nuts. This assembly is suspended on a length of Inconel wire, folded as shown in Fig. 2. The two ends of this wire are inserted into a specially machined stainless steel collet and adjusted such that the cathode assembly is positioned approximately 20 mm below the bottom of the anode. This anode–cathode arrangement was selected as it minimizes the possibility of cyclical reactions between the oxygen bubbles produced at the anode and the partially reduced cathode, as the bubbles float upwards away from the cathode. As the cathode wires pass reasonably close to the anode, alumina sheaths are used to electrically insulate the wires from the electrolyte.

As with the anode, a long electrical connection is needed between the cathode assembly and the power supply. In order to minimize the overall diameter of the cell, a stainless steel tube is used that fits over the alumina sheath surrounding the anode holder. The cathode collet is held in place with a grub screw and the tubular cathode connection is sheathed in another alumina tube. Finally, the whole assembly is bonded into a 1 inch-diameter stainless steel tube which acts as the O-ring surface that seals the cell. This anode–cathode assembly, hereafter referred to as the electrode stalk, allows samples to be easily inserted and removed from the cell, minimizing the time taken to change samples during synchrotron experiments.

2.1.2. Cell body. The cell body is constructed from a closed-end alumina tube (McDanel Ceramics, USA), selected for being inert, robust, inexpensive and relatively X-ray transparent, bonded into a machined aluminium cap using a ceramic cement (Ceramabond 671, Aremco Products) as shown in Fig. 3. This aluminium cap provides a flange with threaded bolt holes, an O-ring groove to ensure a gas-tight seal against the cell head, and a single NPT port for gas supply or extraction. The internal diameter of the cell body accommodates the 1 inch sample stalk with ∼10 mm of clearance radially for ancillary devices such as thermocouples, gas supply tubes and reference electrodes. The overall height of the cell body is 530 mm, which allows 320 g of $CaCl_2$ powder to be loaded, initially occupying ∼290 mm vertically, and subsequently melted down to a vertical height of ∼100 mm. The simplicity of the design allows for easy replacement of the cell body and cap, which are consumable items that typically require replacement after three or four experiments.

2.1.3. Cell head. The machined aluminium cell head (Fig. 4) features all of the feedthrough ports necessary to conduct laboratory-scale electrochemical experiments. The central

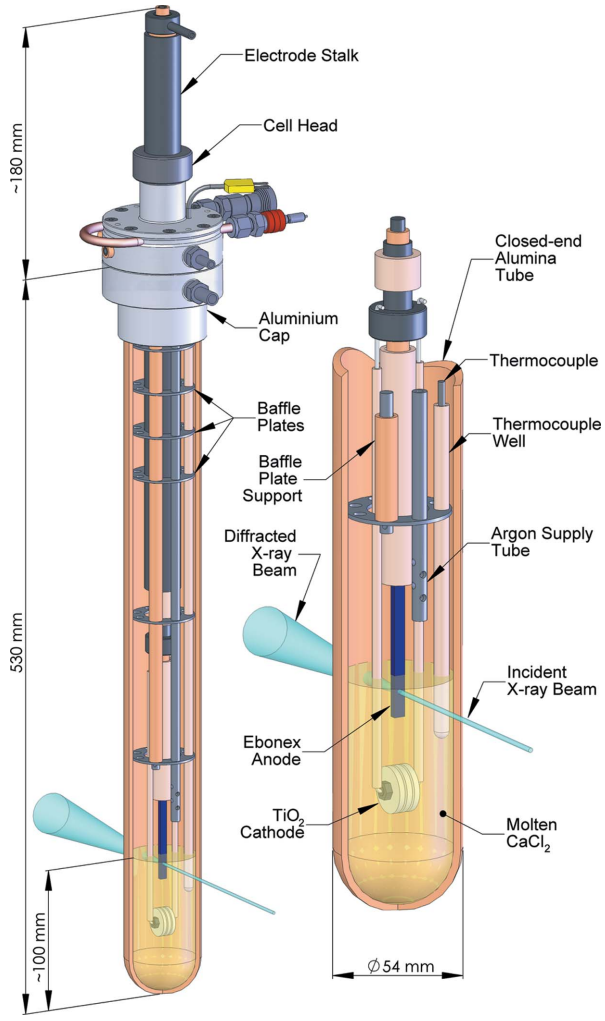

Figure 3
Section view of the molten salt electrowinning cell described in the text, showing key dimensions and features.

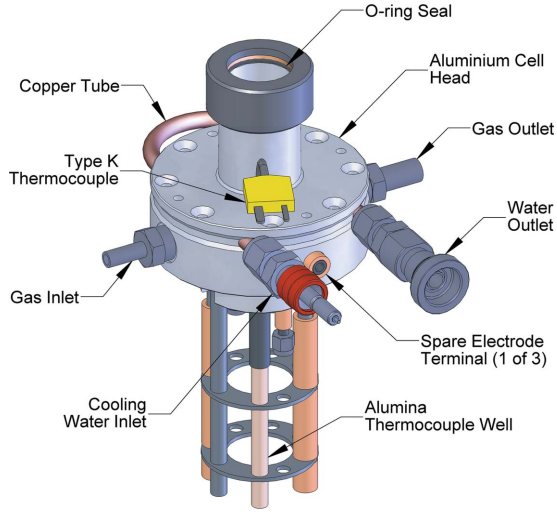

Figure 4
Schematic drawing of the cell head showing the connections available for conducting electrolysis experiments.

port utilizes a 1 inch vacuum-rated quick-connect (MDC Vacuum, USA), which seals onto the outer steel tube of the electrode stalk. This port was designed to ensure that the anode sample would be located within 1 mm of the central axis of the cell, yet allow straightforward and accurate adjustment of anode height and angular position. This feature greatly reduces the amount of time taken to locate the anode sample with the X-ray beam. Two NPT ports, machined into the side of the cell head directly opposite each other, allow argon gas to flow through channels into and out of the cell *via* standard Swagelok-style fittings. An Inconel tube connected to one of these ports is used to transfer the incoming argon to the bottom of the cell, just above the surface of the molten salt. Six Inconel baffle plates are suspended from the cell head to assist in reducing the thermal gradient experienced by samples as they are lowered into position. As the cell head is water cooled *via* a copper cooling channel, the upper baffle plates also act as a form of heat sink which helps to condense $CaCl_2$ vapour and limit the concentration of salt in the off-gas. The cell head also features three additional banana plug terminals that allow electrical connection to fixed devices such as reference electrodes inside the cell.

A thermocouple port is drilled vertically through the cell head next to the central sample port. The bottom of this hole is threaded so that an alumina thermocouple well can be suspended in place. This allows the thermocouple, which is used to directly measure the temperature of the molten salt, to be easily replaced in the event of failure mid-experiment. However, at the conclusion of an electrolysis run the thermocouple well remains suspended in solidified salt, requiring the salt to be washed out with hot water before the cell head can be removed. Future implementations of this cell design will aim to improve this feature, which is hampered by the limited space available on top of the cell head.

2.2. Furnace design

The furnace used to heat the aforementioned cells to operating temperature is shown schematically in Fig. 5. In many ways this furnace resembles other high-temperature equipment that have been reported previously (Evans *et al.*, 1995; Geselbracht *et al.*, 2000; Jackson *et al.*, 2010). However, it is substantially larger, allowing greater flexibility in cell design, and includes a number of features which assist synchrotron experimentation. The key features of the furnace are summarized in Table 1.

2.2.1. Heating elements and power supply. The heating elements are constructed from spiral-wound Kanthal A1 wire attached to an alumina working tube (Alsint, 99.8% Al_2O_3) 400 mm long with a 92 mm internal diameter. The heating elements have been designed to provide upper and lower heating zones each ~200 mm long, which in practise allows a controlled temperature difference of around 250 K between the centres of the two zones. This relatively long heated length is needed to uniformly heat loosely packed powdered salt, which upon melting pools in the bottom third of the electrowinning cell. In order to minimize the total height of the

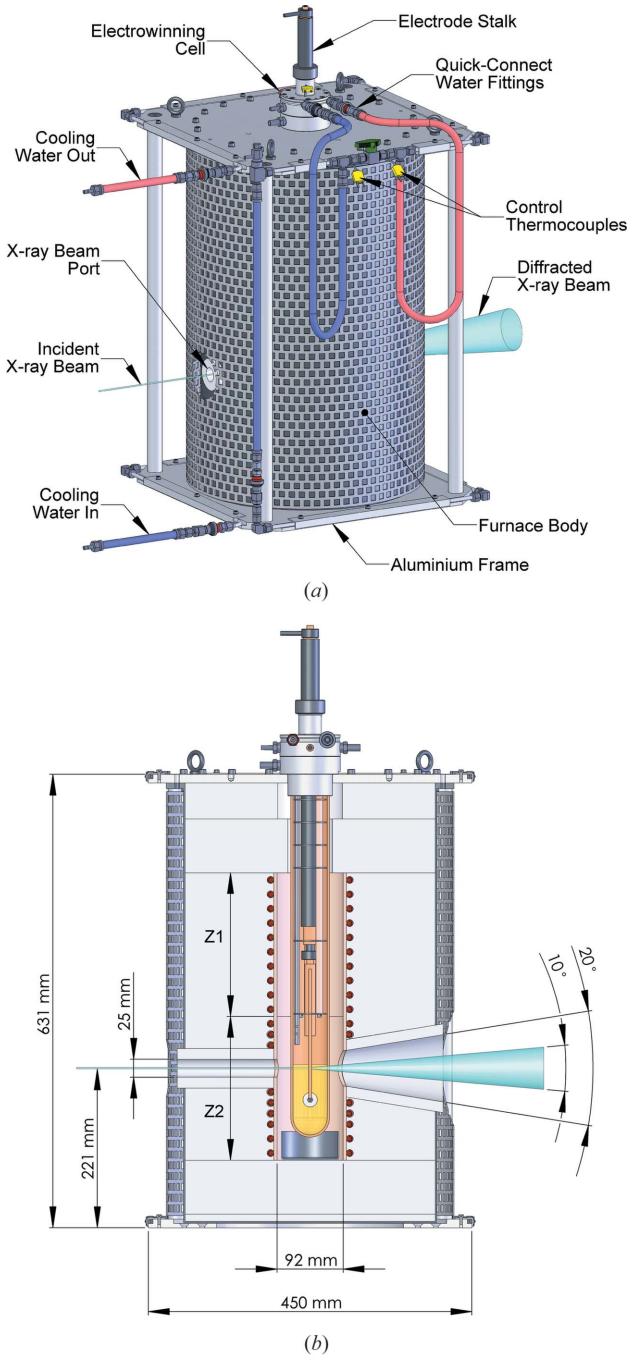

Figure 5
Schematic drawing showing an overview (*a*) and a cross section (*b*) of the furnace. Note the passage of the X-ray beam through the cell and windows. Z1 and Z2 correspond to heating zones 1 and 2, respectively.

furnace, a two-zone arrangement allows the top zone to be switched off after melting has occurred and effectively reduce the thermal gradient experienced by samples as they are lowered into the molten salt. The reduced thermal gradient also helps to condense $CaCl_2$ vapour on the baffle plates and internal walls of the cell, thereby limiting the concentration of the salt in the off-gas.

To ensure that the furnace can be operated at international facilities, the power requirements have been limited to allow the use of a relatively common 240 V AC and 10 A supply. With only 2.4 kW of power available, a substantial amount of insulation is required in order to achieve the maximum operating temperature of 1373 K and maintain accurate control over sample temperatures within the cell. The outside diameter of the furnace is 400 mm which includes a 25 mm air gap between a perforated heat shield and the steel skin of the furnace (which prevents operators from coming in contact with temperatures greater than 308 K), and 120 mm of graded ceramic fibre blanket around the heating elements. The effect of such a large thermal mass is a relatively slow maximum heating rate of 5 K min^{-1} at the sample. However, this is sufficiently fast for simulating many industrial processes including reactive sintering and hydrothermal synthesis.

Table 1
Summary of the specifications for the furnace described in §2.2.

Feature	Specification
Maximum sample temperature	1373 K
Element arrangement	Vertical tube furnace
Total heated length	400 mm nominal
Maximum cell diameter	60 mm
Incident beam port	25 mm diameter
Diffracted beam port	Minimum 10° 2θ
Height of beam ports	221 mm from base
Power supply	240 V AC, 10 A
Maximum heating rate	5 K min^{-1}
Temperature control	±1 K
Maximum surface temperature	308 K
Safety	Independent over-temperature control
Communications	Ethernet and RS232
Weight	Less than 50 kg

2.2.2. X-ray beam ports. To allow the unobstructed passage of X-rays through the furnace, a cylindrical incident beam port and a conical diffracted beam port have been constructed at a fixed height of 221 mm above the base of the furnace (Fig. 5). The size and position of these ports were affected by many factors including thermal losses, maximum cell size and the requirement that the furnace also be compatible with monochromatic X-ray scattering techniques. The dimensions of the diffracted beam port allow entire Debye–Scherrer cones to be observed out to at least 10° 2θ, no matter where the incident beam is positioned relative to the centreline of the incident port. However, this angular range can be extended in certain directions if the incident beam is positioned near the extremities of the incident beam port. During data collection, a single thickness of aluminium foil, which is virtually transparent to X-rays at these energies, can be used as window material to reduce convective heat losses caused by airflow through the beam ports. However, ceramic insulating plugs can be used for both windows to minimize heat loss during the initial ramping stage.

In order to allow reaction vessels to extend down past the height of the X-ray ports, the insulation at the bottom of the furnace has been minimized. To reduce thermal losses, the bottom end of the working tube is blocked off by two vacuum formed ceramic fibreboards, which are supported by the sealed base of the furnace. An Inconel cup has been posi-

tioned at the bottom of the working tube to collect material in the event that a reaction vessel fractures during operation.

2.2.3. Temperature control and communications. Temperature control is achieved using a Eurotherm model 3504 dual-loop controller. This allows the temperature profiles of both zones to be programmed and controlled simultaneously. K-type control thermocouples are positioned inside the working tube in the centre of both heating zones. Measurements from the molten salt cell show that the sample temperature inside an alumina reaction vessel are within 1 K of the control thermocouple temperature, with a lag of about 1 to 5 min depending on the heating rate. An additional two K-type thermocouples are positioned on the outside of the working tube to directly measure the temperature of the heating elements. The temperatures of these thermocouples are monitored by two Eurotherm 3216 controllers which prevent run-away heating of the elements in the event that the main controller fails. These devices are isolated from the main controller, and each other, and activate solid state relays to cut power when element temperatures exceed the maximum safe temperature determined for each experiment. To reduce the weight of the furnace, all controllers and relays are located in a separate control box which can be positioned up to 4 m away from the furnace itself. This also allows the controllers to be shielded from the scattered high-energy X-rays within the experimental hutch.

To allow communication and control of the furnace from outside the experimental hutch, the Eurotherm 3504 controller is fitted with both Ethernet and RS232 communication modules. As the safety protocols at many synchrotron facilities require cables to pass through somewhat lengthy conduits, Ethernet communications can be advantageous over RS232.

2.2.4. Sample positioning *via* an external frame. In order to accurately position a sample within the furnace, an aluminium frame is constructed around the furnace that provides a method of accurately locating the top of the furnace with respect to a calibrated sample stage. This frame is constructed from two 12 mm-thick aluminium plates with four 25 mm-diameter rods connecting top and bottom and features water cooling and lifting collars (to allow for the use of a crane). In order to avoid placing a potentially excessive heat load on a beamline's sample table, the frame has been designed to maintain an air gap between the bottom skin of the furnace and the top of the base plate.

The base plate is also cooled around its periphery to further reduce the chance of over-heating sample stages. Connection to the sample table is *via* four M6 counter-sunk bolts. The overall weight and size of the furnace, including the frame and fittings, is 48 kg and 460 mm × 480 mm by 640 mm.

3. Application to inert anode research

Electrically conductive oxides make appealing candidates as inert replacements for the carbon anode materials currently used in the FFC process, as their high oxygen contents should provide good resistance to corrosion *via* oxidation processes. In particular, electrodes constructed from the Magnéli phases, Ti_nO_{2n-1} (Andersson *et al.*, 1957), are of interest owing to a reduced chance of the corrosion products contaminating the titanium being produced at the cathode. Dense plates consisting of a mixture of the most electrically conductive Magnéli phases (n = 4 to 6) are produced commercially under the brand name Ebonex (Atraverda Ltd) and are successfully employed in a variety of corrosive environments (Hayfield, 2002). However, laboratory trials using Ebonex as an anode in an FFC cell have found that it quickly develops a non-conductive rutile (TiO_2) surface layer, which grows in thickness over a matter of hours until eventually the entire anode is converted to TiO_2 (McGregor *et al.*, 2006). Despite this, Ebonex is a suitable choice for a model inert anode for the FFC process, as it (i) remains dimensionally stable during electrolysis, (ii) does not contaminate the bath or product, (iii) has a well characterized failure mode, and (iv) has a complicated crystal structure which can be used to test the sensitivity of the analysis methodology of Scarlett *et al.* (2009).

3.1. EDXRD experimentation

Beamline I12-JEEP (Joint Engineering, Environmental and Processing) at the Diamond Light Source receives high-energy white X-rays from a 4 T wiggler with a usable energy range of 30–150 keV. The use of high-energy white X-rays allows relatively simple incident beam optics and a simple diffracted beam path to the detector compared with monochromatic instruments, resulting in much higher X-ray flux at the sample. It also provides very high beam penetration and thus makes the beamline suitable for examining relatively large samples.

The diffracted X-rays are measured using a semi-annular array of 23 liquid-nitrogen-cooled germanium energy-sensitive detectors 2 m from the sample position at an angle of 5° 2θ from the incident beam (see Fig. 6*b*). The relative energy resolution of the Ge detector ranges from 7×10^{-3} at 50 keV to 4×10^{-3} at 150 keV. The diffracted beam is collimated by a set of two slits: a 150 µm semi-annular slit 551 mm from the sample position and a series of 250 µm slits immediately in front of each detector. The available energy range and 5° detector angle allow Bragg reflections with d-spacings in the range 0.95–4.7 Å to be observed.

The volume of the sample from which diffraction information is obtained is referred to as the 'active' volume, and is defined by the intersection of the paths of the incident beam and the detector collimators. This intersection creates a lozenge-shaped area of investigation (Fig. 1) which is fixed in space, and the sample can be scanned through it in order to obtain diffraction information from different parts of the sample. The length of this lozenge (L) can be calculated for both parallel and divergent beam instruments using the equations described by Rowles (2011).

Fig. 6(*a*) shows the furnace mounted on the JEEP sample table which is modular, allowing different motion stages to be removed in order to position larger samples or support heavier loads. In the experiment described here the furnace control box was positioned near the base of the sample table,

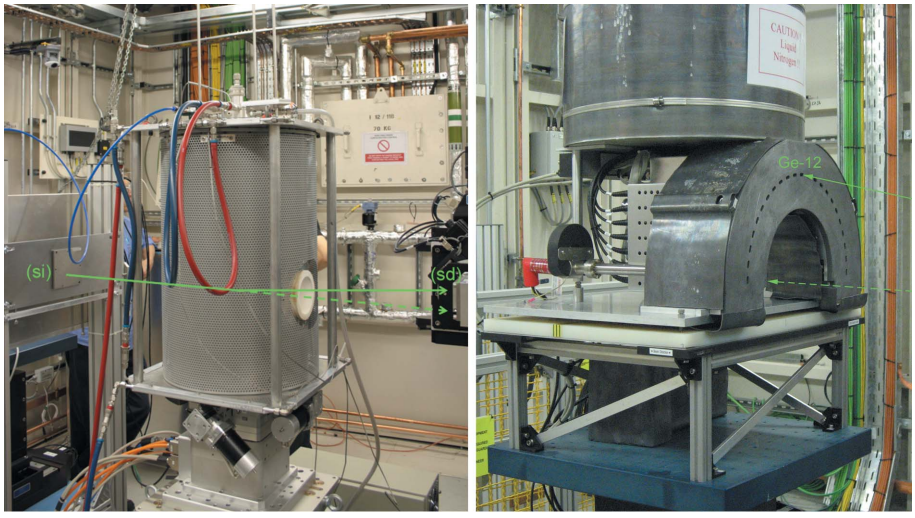

(*a*) (*b*)

Figure 6
In part (*a*) the furnace is shown mounted on the JEEP translation table along with the molten salt electrowinning cell. The X-ray beam (indicated by the green arrows) enters from the left through the slits marked (si). The analysis volume is selected by the slits just visible on the right at (sd). Part (*b*) shows the energy-dispersive detector system consisting of a semi-annular array of 23 liquid-nitrogen-cooled germanium energy-sensitive detectors 2 m from the sample position at an angle of 5° 2θ from the incident beam. The central detector (Ge-12) is labelled.

while the electrochemical equipment was positioned in a beamline-supplied lead-lined cabinet.

3.2. Electrolyses

Electrolyses were conducted by applying a constant current supplied by a PAR model 362 scanning potentiostat fitted with a PAR model 365 current booster. The current was ramped at 1.75 A h^{-1} until the operating current was reached. Cell voltage, current and electrolyte temperature were measured and recorded every second. Bar-shaped Ebonex anodes 3 × 5 × 75 mm were dipped into the electrolyte to give an exposed area of approximately 3.5 cm^2. The tests were conducted under an argon cover gas (ultra-high purity, 99.999%) in a $CaCl_2$ electrolyte containing 0.2–0.5 wt% CaO, at a temperature of ~1223 K and an anode current of 0.7 A (~0.2 A cm^{-2}).

3.3. Data collection

EDXRD data were collected from anodes over an energy range of approximately 6–160 keV, with useful intensities from 30 to 120 keV. Diffraction data from all 23 detectors were obtained as a function of time from a single point on each anode, with individual data sets being collected for 60 s, with a 5 s delay between consecutive datasets, for ~8 h or until anode failure. The arrangement of the anode in the incident beam is shown in Fig. 3. The active volume for each diffraction pattern was 1 × 1 mm perpendicular to the beam and ~15 mm long in the direction of the incident beam. The 3 mm-thick anode was positioned in the centre of this active volume.

Data were collected at two different points: 7 mm above and 3 mm below the surface of the electrolyte. Data were collected from above the electrolyte to remove the effect of X-ray absorption owing to a long path length in the electrolyte. This still produces valid diffraction information as the liquid electrolyte wicks up the outer surface of the anode, thus enabling electrolysis to occur (McGregor *et al.*, 2007).

3.4. Results

Representative diffraction patterns for data collected above and below the electrolyte surface are shown in Fig. 7. A time-series of diffraction patterns collected above the electrolyte surface is also shown in Fig. 8. All diffraction patterns were

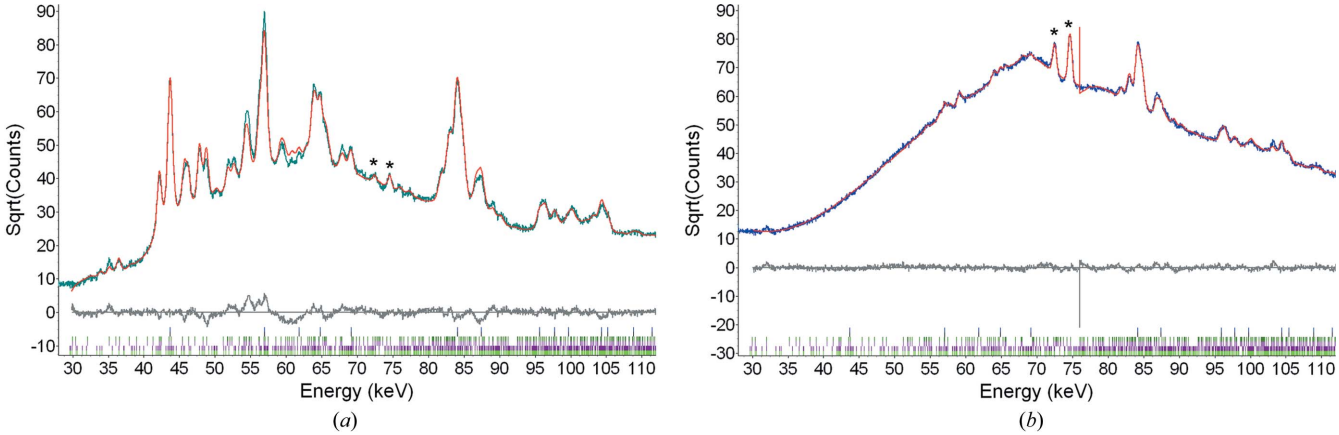

(*a*) (*b*)

Figure 7
Representative diffraction patterns collected (*a*) 7 mm above the surface of the electrolyte, and (*b*) 3 mm below. The calculated diffraction pattern is shown in red, with the difference plot shown in grey. The absorption of lower-energy X-rays by the electrolyte is evident in (*b*). The data presented are from a stage in the reaction when the three phases Ti_5O_9, Ti_6O_{11} and TiO_2 were present at approximately 33 wt% each. Note that the two starred peaks in both (*a*) and (*b*) are due to lead *K*-fluorescence from the detector shielding and, as such, do not vary in intensity with time.

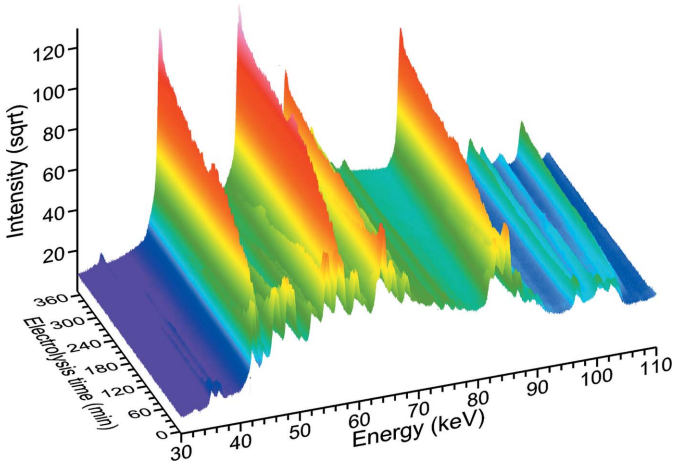

Figure 8
A time series of diffraction patterns collected 7 mm above the surface of the electrolyte. The growth of peaks associated with the rutile phase can be seen clearly (after Rowles *et al.*, 2011*b*).

collected using the central detector of the array, for a period of 60 s each. Above the surface of the electrolyte, excellent intensities are observed for peaks resulting from energies as low as 40 keV. Below the surface the intensity of peaks resulting from energies less than 80 keV is significantly reduced owing to the heavy absorption of lower-energy X-rays in the molten electrolyte. However, higher-energy peaks remain visible. The only phases observed at the two positions are the Magnéli phases Ti_5O_9 and Ti_6O_{11} and rutile, and their relative abundance is in accordance with *ex situ* measurements. These data have been analysed following the methodology of Scarlett *et al.* (2009) and have been published elsewhere (Rowles *et al.*, 2011*b*). This analysis procedure models X-ray absorption, the incident beam spectrum and the variance of structure factors as a function of energy, allowing for a full crystal-structure-based Rietveld refinement to be undertaken.

4. Prospects for other high-temperature environments

The equipment and methodology described here can easily be applied to a range of other high-temperature processes which, owing to their complexity, are difficult to study using more conventional diffraction techniques. Specific examples include reactive sintering of iron ore fines, intercalation processes in ternary carbides, and pressure acid leaching of minerals. These systems feature three different chemical environments (reducing atmosphere, vacuum and acidic, respectively), and the ability to study these systems using high-energy X-ray diffraction may require reaction vessels that differ significantly from the one described here. However, in many cases the key difference in simulating these environments is simply the material used to construct the reaction vessel. For example, if the Hall–Héroult process was the system of interest the alumina crucible would need to be substituted (owing to its solubility in cryolite) for another material such as graphite. Whilst it is important to allow for the effect that different construction materials will have on the absorption of the X-ray beam, it should be noted that certain materials allow for improved cell geometries, which can be used to compensate for increased X-ray absorption.

As the furnace described here is a closed end tube arrangement with no access *via* the bottom or sides, the entire reaction vessel must be loaded from the top. The maximum diameter of reaction vessels is limited to 60 mm and the most convenient way to locate a vessel is to design a cap compatible with the 62 mm hole centrally located on the top plate of the furnace. As heat will be conducted up through the vessel to the top plate, the cap of the vessel must be water cooled and feature quick-connect fittings compatible with the Swagelok fittings currently available on the furnace. While experiments to date have shown that the temperature of samples are within 1 K of the temperature measured by the control thermocouple, future reaction vessels should continue to feature their own thermocouple to independently measure sample temperature. This is particularly important if the reaction being monitored is significantly exo- or endothermic.

5. Summary

This paper has described the design and construction of a new molten salt cell and furnace, which together allow individual cell components such as anodes and cathodes to be studied *in situ* using synchrotron-based energy-dispersive X-ray diffraction. The performance of this equipment has been demonstrated by an *in situ* study of a model inert anode within an operational Fray–Farthing–Chen Cambridge titanium electrowinning cell, using the JEEP beamline at the Diamond Light Source. Diffraction patterns acquired from both above and below the surface of the electrolyte are of sufficiently high quality to quantitatively determine the phase composition of the anode as a function of time. Furthermore, it has been discussed how this new equipment could be applied to the investigation of a range of other high-temperature processes *via* minor modifications to the cell design.

We acknowledge travel funding provided by the International Synchrotron Access Program (ISAP) managed by the Australian Synchrotron. The ISAP is an initiative of the Australian Government being conducted as part of the National Collaborative Research Infrastructure Strategy. This research was undertaken on the I12-Joint Engineering, Environmental and Processing beamline at the Diamond Light Source, Oxfordshire, UK. We would like to thank beamline scientists Drs Thomas Connolley, Christina Reinhard and Michael Drakopolous for their support during our experiment. This work was conducted as part of doctoral studies undertaken through the University of Melbourne. MJS gratefully acknowledges receipt of a full PhD scholarship from the CSIRO Flagship Collaboration Fund, and additional funding from the CSIRO Light Metals Flagship which has made this work possible. We would like to thank the mechanical workshops at CSIRO and The University of

Melbourne, and Tetlow Kilns and Furnaces for their efforts in the construction of the cell and furnace.

References

Andersson, S., Collén, B., Kuylenstierna, U. & Magnéli, A. (1957). *Acta Chem. Scand.* **11**, 1641–1652.

Barnes, P., Clark, S. M., Hausermann, D., Henderson, E., Fentiman, C. H., Rashid, S. & Muhamad, M. N. (1992). *Phase Transit. A*, **39**, 117–128.

Bertolini, M., Shaw, L., England, L., Rao, K., Deane, J. & Collins, J. (2010). *Key Eng. Mater.* **436**, 75–83.

Buras, B., Olsen, J. S. & Gerward, L. (1976). *Nucl. Instrum. Methods*, **135**, 193–195.

Cheetham, A. K. & Mellot, C. F. (1997). *Chem. Mater.* **9**, 2269–2279.

Chen, G. Z., Fray, D. J. & Farthing, T. W. (2000). *Nature (London)*, **407**, 361–364.

Clark, S. M. (2002). *Crystallogr. Rev.* **8**, 57–92.

Clark, S. M., Nield, A., Rathbone, T., Flaherty, J., Tang, C. C., Evans, J. S. O., Francis, R. J. & O'Hare, D. (1995). *Nucl. Instrum. Methods Phys. Res. B*, **97**, 98–101.

Dow Chemical Company (1997). *Development of an Inert Ceramic Anode to Reduce Energy Consumption in Magnesium Production*, Report DOE/ID/13133. Dow Chemical Company, Midland, MI, USA.

Evans, J. S. O., Francis, R. J., O'Hare, D., Price, S. J., Clark, S. M., Flaherty, J., Gordon, J., Nield, A. & Tang, C. C. (1995). *Rev. Sci. Instrum.* **66**, 2442–2445.

Evans, J. W. (2007). *JOM*, **59**, 30–38.

Francis, R. J. & O'Hare, D. (1998). *J. Chem. Soc. Dalton Trans.* pp. 3133–3148.

Fray, D. (2001). *JOM*, **53**, 26–31.

Fray, D. J. (2008). *Intl Mater. Rev.* **53**, 317–325.

Galasiu, I., Galasiu, R. & Thonstad, J. (2007). *Inert Anodes for Aluminium Electrolysis.* Aluminium-Verlag.

Geselbracht, M. J., Walton, R. I., Cowell, E. S., Millange, F. & O'Hare, D. (2000). *Rev. Sci. Instrum.* **71**, 4177–4181.

Ginatta, M. (2000). *JOM*, **52**, 18–20.

Habashi, F. (1997). *Handbook of Extractive Metallurgy.* Weinheim: Wiley-VCH.

Häusermann, D. & Barnes, P. (1992). *Phase Transit. A*, **39**, 99–115.

Hayfield, P. C. S. (2002). *Development of a New Material: Monolithic Ti_4O_7 Ebonex Ceramic.* Cambridge: Royal Society of Chemistry.

Jackson, B. K., Dye, D., Inman, D., Bhagat, R., Talling, R. J., Raghunathan, S. L., Jackson, M. & Dashwood, R. J. (2010). *J. Electrochem. Soc.* **157**, E57–E63.

Jiao, S. & Fray, D. (2010). *Metall. Mater. Trans. B*, **41**, 74–79.

Kraft, E. H. (2004). *Summary of Emerging Titanium Cost Reduction Technologies.* Vancouver: EHK Technologies.

Kroll, W. (1940). *Trans. Electrochem. Soc.* **78**, 35–47.

McGregor, K., Frazer, E. J., Urban, A. J., Pownceby, M. I. & Deutscher, R. L. (2006). *ECS Trans.* **2**, 369–380.

McGregor, K., Urban, A. J. & Frazer, E. J. (2007). *Proceedings of the 11th World Conference on Titanium*, edited by M. Niinomi, S. Akiyama, M. Hagiwara, M. Ikeda and K. Maruyama, pp. 127–130. Sendai: The Japan Institute of Metals.

Norby, P., Hanson, J. C., Fitch, A. N., Vaughan, G., Flaks, L. & Gualtieri, A. (2000). *Chem. Mater.* **12**, 1473–1479.

Pawlek, R. (2008). *Light Metals*, **2008**, 1039–1045.

Pawlek, R. (2010). *Light Metals*, **2010**, 377–382.

Riley, D. P., Kisi, E. H., Hansen, T. C. & Hewat, A. W. (2002). *J. Am. Ceram. Soc.* **85**, 2417–2424.

Rowles, M. R. (2011). *J. Synchrotron Rad.* **18**, 938–941.

Rowles, M. R., Scarlett, N. V. Y., Madsen, I. C. & McGregor, K. (2011*a*). *J. Appl. Cryst.* **44**, 853–857.

Rowles, M. R., Styles, M. J, Madsen, I. C., Scarlett, N. V. Y., McGregor, K., Riley, D. P., Snook, G. A., Urban, A. J., Connolley, T. & Reinhard, C. (2011*b*). *J. Appl. Cryst.* Accepted.

Scarlett, N. V. Y., Madsen, I. C., Evans, J. S. O., Coelho, A. A., McGregor, K., Rowles, M., Lanyon, M. R. & Urban, A. J. (2009). *J. Appl. Cryst.* **42**, 502–512.

Scarlett, N. V. Y., Madsen, I. C. & Whittington, B. I. (2008). *J. Appl. Cryst.* **41**, 572–583.

Styles, M. J. & Riley, D. P. (2010). *J. Phys. Conf. Ser.* **251**, 012089.

Styles, M. J., Riley, D. P., Christoforidis, J. & Olsen, S. (2009). *Z. Kristallogr. Suppl.* **30**, 201–206.

Walton, R. I. & O'Hare, D. (2000). *Chem. Commun.* pp. 2283–2291.

Zhang, H., De Nora, V. & Sekhar, J. A. (1994). *Materials Used in the Hall–Heroult Cell for Aluminum Production.* Warrendale: Minerals, Metals and Materials Society.